Supporting Information

1. Core Formation Modeling

Core formation was modeled as a multi-stage process occurring during accretion, in a terrestrial magma ocean, adapted from Wood and Wade. The Earth, which is covered by a magma ocean, grows by accretion, during which the molten metal of the accretionary material separates form the molten silicate. The metal sinks to the base of the magma ocean, acquires a particular composition by equilibrating with the surrounding magma ocean, and is then transported to the core through the solid mantle with no (or little) further equilibration. At the end of accretion, the core and mantle have acquired a certain composition, which is the integral of this process.

The multi-stage model was discretized in 1000 steps, each bringing an additional 0.1% total Earth mass influx to the proto-Earth. At each step, the Earth grows larger, the magma ocean grows deeper, and its pressure and temperature increase, and its composition changes because of the mass influx. All these parameters are used to calculate metal-silicate partition coefficients, in turn used to calculate element concentrations in the metal and silicate. These are then used to calculate the integral path and the final composition of the core and mantle. The elements we focused on in this study are 4 siderophile trace elements: Ni, Co, Cr, and V. and the two major elements that tend to partition into metallic iron at high temperatures: O and Si.

As described below, we explored all possible magma ocean depths (from 0 to 100% of the mantle), all possible geotherms relevant to the base of that magma ocean (temperatures between the mantle solidus and liquidus), and magma ocean compositions spanning 4 orders of magnitudes in oxygen fugacity and covering the entire range of the cosmochemically observed compositional range for planetary building blocks (ordinary, carbonaceous, and enstatite chondrites).

a. Metal-Silicate Partitioning

Metal-silicate partitioning was modeled based on a compilation of data in the literature, Siebert et al. and references therein.

The partition coefficients are defined as:

$$D_i = \frac{X_i^{metal}}{X_i^{silicate}} \qquad \text{(Eqn. 1)}$$

where *i* is Ni, Co, Cr, V, Si, or O; and X the molar concentrations in the metal or silicate. They are parameterized as follows:

$$\log(D_i) = a + \frac{b}{T} + c\frac{P}{T} - \frac{n}{2}\log\frac{X_{FeO}^{silicate}}{X_{Fe}^{metal}} - \log\gamma_i + \frac{n}{2}\log\gamma_{Fe} \qquad \text{(Eqn. 2)}$$

where a, b, and c are regression constants corresponding to entropy, enthalpy, and volume terms; X_{FeO} and X_{Fe} are the FeO concentration in the silicate and Fe concentration in the metal, respectively; n is the valence of element i (i=Ni, Co, Cr, V, Si, O); γ_i and γ_{Fe} are the activity coefficient (in the metal) of element i (i=Ni, Co, Cr, V, Si, O) and iron, respectively. Those were calculated using the interaction parameter approach (1), and self-consistently evolve along with the composition of the metal. This approach allows the use of interaction parameters ε to calculate the activity of multicomponent metallic solutions. In a metallic solution containing N components, the activity coefficients of Fe and the N-1 solutes (i) is given by:

$$\begin{aligned}\ln\gamma_{\mathrm{Fe}} &= \sum_{i=1}^{N-1}\varepsilon_i^i(X_i+\ln(1-X_i))\\ &-\sum_{j=1}^{N-2}\sum_{k=j+1}^{N-1}\varepsilon_j^k X_j X_k\left(1+\frac{\ln(1-X_j)}{X_j}+\frac{\ln(1-X_k)}{X_k}\right)\\ &+\sum_{i=1}^{N-1}\sum_{\substack{k=1\\(k\neq i)}}^{N-1}\varepsilon_i^k X_i X_k\left(1+\frac{\ln(1-X_k)}{X_k}-\frac{1}{1-X_i}\right)\\ &+\frac{1}{2}\sum_{j=1}^{N-2}\sum_{k=j+1}^{N-1}\varepsilon_j^k X_j^2 X_k^2\left(\frac{1}{1-X_j}+\frac{1}{1-X_k}-1\right)\\ &-\sum_{i=1}^{N-1}\sum_{\substack{k=1\\(k\neq i)}}^{N-1}\varepsilon_i^k X_i^2 X_k^2\left(\frac{1}{1-X_i}+\frac{1}{1-X_k}+\frac{X_i}{2(1-X_i)^2}-1\right)\end{aligned} \qquad \text{(Eqn. 3)}$$

and

$$\begin{aligned}\ln\gamma_i &= \ln\gamma_{\mathrm{Fe}}+\ln\gamma_i^0-\varepsilon_i^i\ln(1-X_i)\\ &-\sum_{j=1(j\neq i)}^{N-1}\varepsilon_{\mathrm{i}}^j X_j\left(1+\frac{\ln(1-X_j)}{X_j}-\frac{1}{1-X_i}\right)\\ &+\sum_{j=1(j\neq i)}^{N-1}\varepsilon_{\mathrm{i}}^j X_j^2 X_i\left(\frac{1}{1-X_i}+\frac{1}{1-X_j}+\frac{X_i}{2(1-X_i)^2}-1\right)\end{aligned} \qquad \text{(Eqn. 4)}$$

Values of the ε_i^j and are reported at a reference temperature of 1873 K (Table 1) and extrapolated to any temperature according to:

$$\varepsilon_i^j(T)=\frac{T_0}{T}\cdot\varepsilon_i^j(T_0)$$

Table S1 below lists all the regression parameters used in our model along with their uncertainties. The regressions are from (2, 3), and were regressed on a large set of previously published data obtained from piston-cylinder press, multi-anvil press, and laser-heated diamond anvil cell experiments.

Element (i)	a	b (K)	c (K/GPa)	ε_i^O (T_0)	ε_i^{Si} (T_0)	ln γ_i^0 (T)
Ni	0.304 (0.162)	2916 (344)	-60 (5)	1.40	1.16	-0.42 * 1873/T
Co	0.287 (0.141)	1360 (286)	-35 (5)	1.89	0	-0.60 * 1873/T
Cr	0.082 (0.097)	-3379 (220)	0	-7.2	0	0
V	-1.238 (0.141)	-5288 (408)	0	-21.1	2.00	-2.53 * 1873/T
Si	0.364 (0.28)	-16520 (716)	0	-5	12.41	-6.65 * 1873/T
O	2.736 (0.14)	11439 (387)	0	-1	-5	4.29 – 16500/T

b. Accretion and Magma Ocean

The Earth was iteratively (discretely) accreted in N=1000 steps, each amounting to 0.1% of Earth's total mass. At each step, the mass and accreted fraction are calculated:

$$M_i = M_{i-1} + \delta M_i \quad \text{and} \quad f_i = \frac{M_i}{M_E} \qquad \text{(Eqn. 5)}$$

and M_i is the mass of the proto-Earth at step i, δM_i the mass flux at step i, and M_E the final mass of the Earth. We used N=1000 and a constant δM_i = 0.001 M_E

As accretion proceeds, the pressure and the temperature at the base of the magma ocean increase. The pressure at the base of the magma ocean is calculated according to:

$$P_i = P_{final} \cdot f_i^{2/3} \qquad \text{(Eqn. 6)}$$

where P_{final} is the pressure at the base of the magma ocean at the end of accretion (f_N=1), or in other words, the final pressure of the magma ocean. P_{final} is an adjustable parameter of the model.

At the base of the magma ocean, the top molten part is in equilibrium with the bottom solid part. Therefore, the temperature at the base of the magma ocean has to lie above the solidus and below the liquidus of pyrolite. We have chosen 4 geotherms based on experimental melting data: the solidus (Eqn. 7) and liquidus (Eqn. 8) from Fiquet et al 2010, the liquidus (Eqn. 9) of Andrault et al 2011, and an intermediate liquidus (Eqn. 10) obtained from the arithmetic mean of the (Eqn. 8) and (Eqn. 9)

$$T_i = 1621 + 38.415P_i - 0.1958P_i^2 + 3.8369 \cdot 10^{-4} P_i^3 \quad \text{(Eqn. 7)}$$

$$T_i = 2022 + 54.21P_i - 0.34P_i^2 + 9.0747 \cdot 10^{-4} P_i^3 \quad \text{(Eqn. 8)}$$

$$T_i = 1940 \left(\frac{P_i}{29} + 1 \right)^{\frac{1}{1.9}} \quad \text{(Eqn. 9)}$$

$$T_i = \frac{1}{2} \left(2022 + 54.21P_i - 0.34P_i^2 + 9.0747 \cdot 10^{-4} P_i^3 + 1940 \left(\frac{P_i}{29} + 1 \right)^{\frac{1}{1.9}} \right) \quad \text{(Eqn. 10)}$$

Finally, at each step, FeO content of the magma ocean is calculated along *ad hoc* models shown in the main article, Figure 1.

c. Core and Mantle Composition

At each accretion step, the pressure, temperature and FeO content of the magma ocean are calculated at its base (eqs. 2–5 and figure 1). These parameters, P_i, T_i, and X_i^{FeO} are the used to calculate the composition of the metal and that of the silicate at equilibrium. The metal is added to the pre-existing core, the silicate magma ocean grows and changes, and the process is repeated.

The concentrations of Ni, Co, Cr, V, Si and O in the metal and silicate are calculated at each step using published partition coefficients and thermodynamical models. The metal is then extracted and added to the pre-existing core, thus changing its composition. The magma ocean composition is also modified, and a new accretion step proceeds.

It is clear that all parameters have associated uncertainties that can be fairly large. It was recently argued that if these uncertainties are properly propagated, core formation can take place in almost any accretion scenario, an even in a single stage! We therefore forward-propagated all uncertainties on the thermodynamic parameters governing the partitioning equations, using Monte Carlo simulation. At each accretion step *i*, 10^5 partition coefficients are calculated according to equation 7, where the parameters *a*, *b*, and *c* are sampled from a normal distribution around their mean and standard deviation. This means that we obtain the full statistical dispersion for each partition coefficient, which is only possible with the use of Monte Carlo Simulations. The average partition coefficient and its (1-σ) standard error are then obtained from the statistics on those 10^5 values of D, effectively propagating the uncertainties in thermodynamic parameters on the metal-silicate partition coefficients. Then the 1-σ values were used to obtain the figure in the main article, and can be compared with the same plot obtained by using 2-σ is shown in Fig. S1. It is clear that the solution spaces naturally occupy a larger extent, but the message is the same. Highly reduced models (paths 1-5) still cannot yield core compositions that are consistent with seismology, whereas the most oxidized models (path 13 and 14) can be made consistent at the lower end of the P–T range of equilibration. At any rate, relaxing the uncertainties cannot help reconcile the seismic models with cores produced under reducing conditions in the magma ocean.

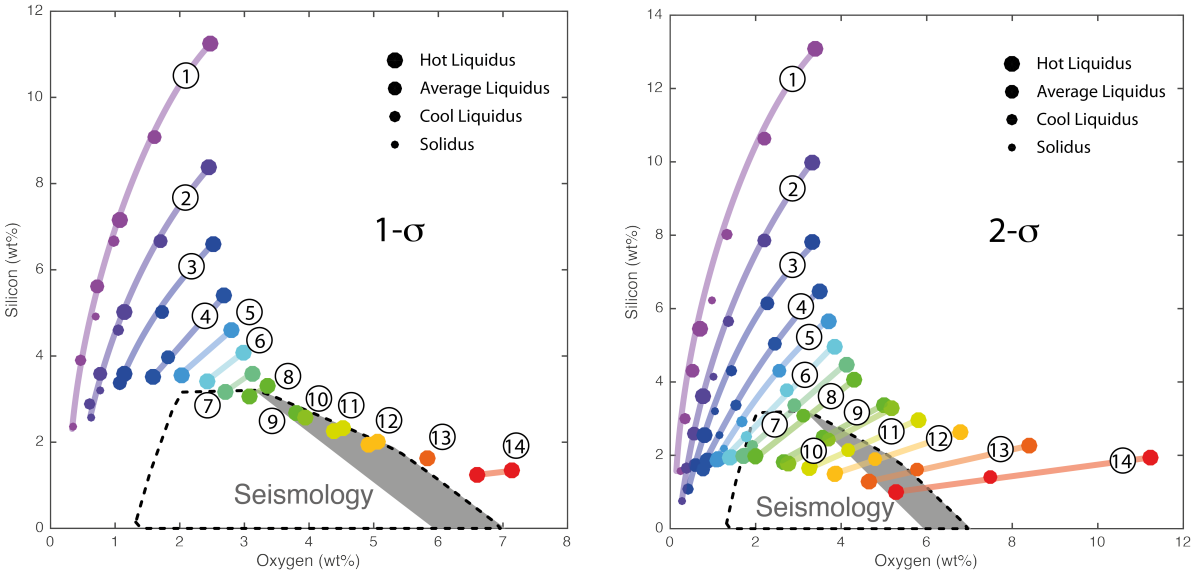

Figure S1: (Left) The same plot as Fig. 2 in the main text. The points represent the spread of the solutions obtained by propagating all uncertainties in the partition coefficients to 1-σ. The seismologically consistent composition space consists of the area delimited by the black dashed line; the grayed sub-area corresponding to the O and Si solutions if the core contains no C and no S, and the rest of the polygon corresponding to the O and Si solutions with a core containing up to 2% S and 5% C. (Right) A similar plot obtained by propagating all uncertainties in the partition coefficients to 2-σ instead of 1-σ. The spreads are naturally larger, but the highly reduced models (paths 1-5 in ig. 1) still cannot produce core compositions that satisfy seismology. The main difference is that the most oxidized paths (13 and 14) that couldn't produce geophysically acceptable cores now do.

d. Model Output

The model's output is the evolution of partition coefficients (Ni, Co, Cr, V) and Si and O content in the metal, as a function of accreted fraction. Figure S3 below shows a typical example of such a multi-stage core formation model, for a final magma ocean pressure of 65 GPa, a warm liquidus, and accretion path 6 (intial FeO concentration in the magma ocean is 8 mol%) from Figure 1.

The next step is to focus solely on the final values, reached at the end of accretion, since these are the ones that will be used to constrain the model. We successively ran 136 simulations such as the one described above, varying P_{final} between 0 and 135 GPa, by 1 GPa increments. The final values (Ds and core compositions) at the end of accretion are then plotted as a function of final magma ocean pressure, as shown in figure S3. Again, the solid lines are the Monte Carlo averages of the D distributions, and the dashed lines are the 1-sigma envelopes.

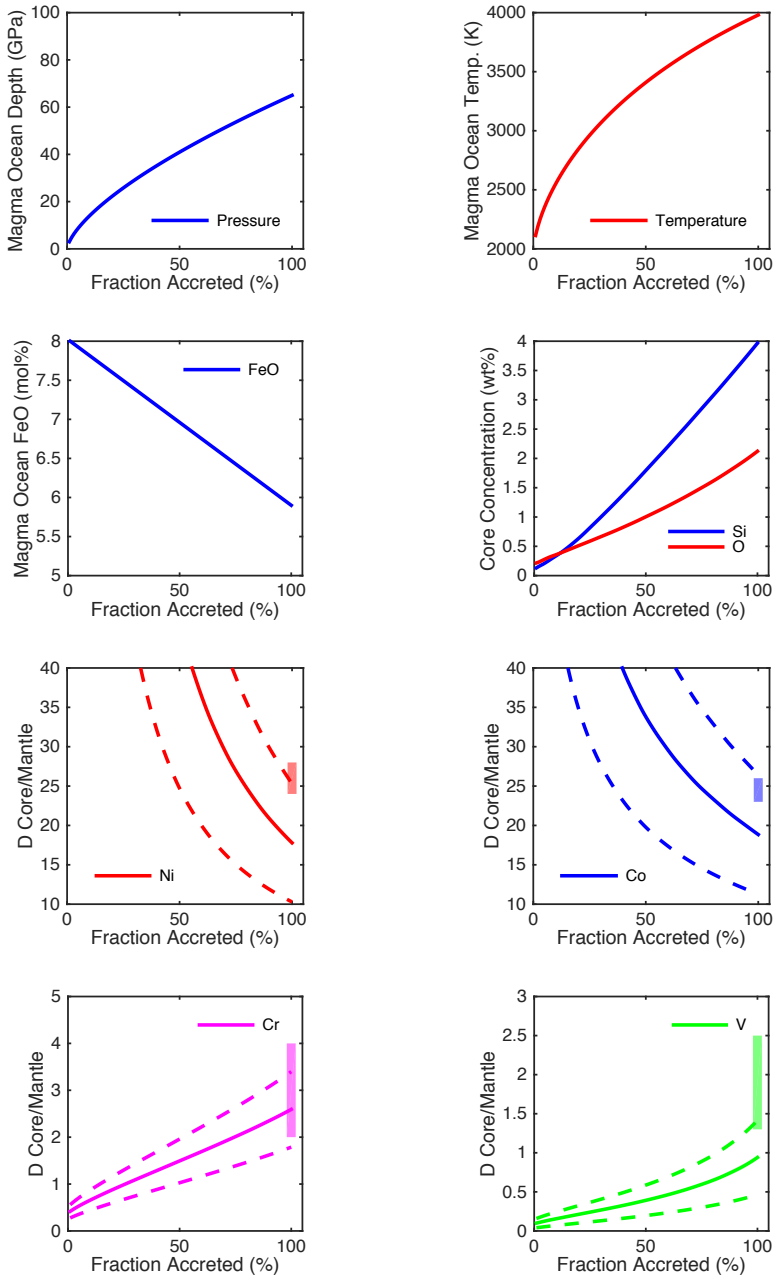

Figure S2: Evolution of thermodynamic parameters in the magma ocean and core. The top 4 panels represent the evolution of thermodynamic conditions in the magma ocean as a function of accreted fraction: pressure (blue), temperature (red), redox (green), and O/Si concentration in the core. The bottom 4 panels show the evolution of the core-mantle partition coefficients of the four siderophile elements (Ni in red, Co in blue, Cr in violet, V in green) as a function of accreted fraction; the solid line corresponds to the Monte Carlo average and the dashed lines to the 1-sigma envelope. The vertical bar corresponds to the observed core-mantle partition coefficient (with its uncertainty), and represents the value, or range of values, that must be reached at the end of accretion for the model to match the observation.

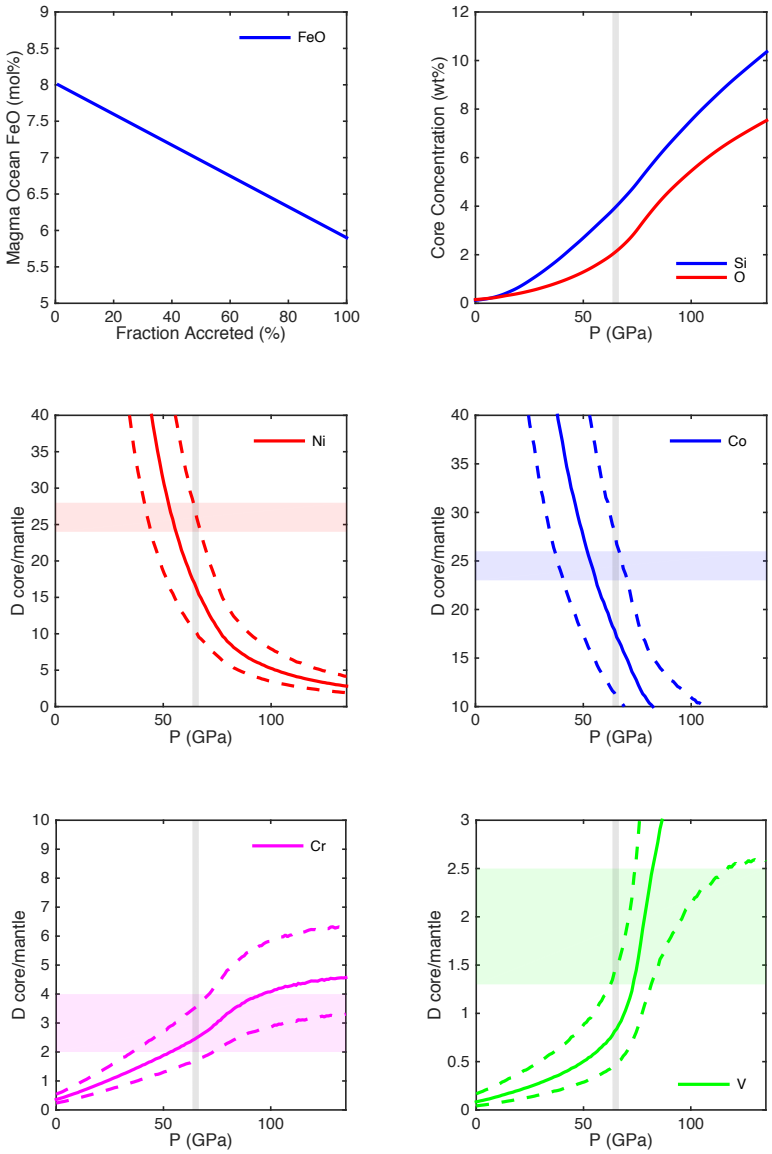

Figure S3: The result of a series of multi-stage core formation models where the final magma ocean depth (or pressure) was varied from 0 to 135 GPa, scanning the whole possible range of plausible magma oceans pressure in the Earth. We used the same redox path ad geotherm as in the example shown in figure S2. Each point in this graph corresponds to the endpoint of the graphs in figure S2, computed for different final pressures. Note that the same numbers are found at the end of accretion in figure S2 and at 65 GPa in this figure. Notice that the x-axis (except for the redox model on the top left) is now labeled in GPa, corresponding to final magma ocean depth. The Ds and core concentrations are the final values reached at the end of accretion. The horizontal shaded areas correspond to the terrestrial observables, and these are the same as the bars in figure S2. The vertical bar corresponds to the pressure range for which all four partition coefficients match the observables, and therefore constrains the locus of plausible magma ocean depths for a given redox and geotherm.

For a given geotherm and a given composition, this allows constraining the depth range of the magma ocean that would be consistent with the geochemical observables (horizontal colored range). Since all four partition coefficients need to be satisfied simultaneously, the allowable P range (vertical gray range) corresponds to the intersection of all four pressure ranges. Each one of those simulations provides an acceptable pressure (or depth) range for the magma ocean, as well as a concentration range for O and Si in the core; these satisfy Ni, Co, Cr, and V abundances in the mantle, for a given geotherm and a given redox path.

Taking this idea one step further, all geotherms and all redox paths were tested. We now solely focus on the O and Si concentrations in the core within the gray vertical bar (top right panel in figure S3), *i.e.* in P–T–fO_2 conditions that satisfy the mantle concentrations for Ni, Co, Cr, and V. These values of Si and O are plotted one against another for various geotherms and redox paths, and these are reported in the main text in figure 2.

Table S1: Model outputs of multi-stage core formation model for which Ni, Co, V, and Cr concentrations in the mantle match the present-day geochemical observables. The table is similar to Table 1 in the main text but has additional info. The data is given for each redox path (Fig. 1) and each geotherm, and empty cells indicate that there is no solution for the relevant redox/geotherm pair. Final pressure (top left), temperature (top center), and depth (top right) range of the magma ocean at the end of accretion. Average pressure (center left) and temperature (center) averaged over accretion. Final oxygen (bottom left) and silicon (bottom center) concentrations in the core; along with total light element concentration (bottom right) at the end of core formation.

Table S2

			Magma Ocean Pressure (at base, at end of accretion) (GPa)								Magma Ocean Temperature (at base, at end of accretion) (K)								Magma Ocean Depth (at end of accretion) (km)							
Path	Initial Redox	Initial FeO (mol%)	Solidus		Cool Liquidus		Average Liquidus		Hot Liquidus		Solidus		Cool Liquidus		Average Liquidus		Hot Liquidus		Solidus		Cool Liquidus		Average Liquidus		Hot Liquidus	
1	IW-4.5	0.6	49	75	48	74	46	71	43	65	3078	3563	3243	3780	3541	4102	3796	4358	1221	1768	1208	1748	1165	1687	1100	1565
2	IW-4.5	0.6	66	75	54	74	45	71	43	64	3414	3563	3374	3780	3516	4102	3796	4336	1586	1768	1336	1748	1144	1687	1100	1545
3	IW-3.3	2			73	73	53	70	42	64			3760	3760	3714	4082	3766	4336			1728	1728	1315	1668	1079	1545
4	IW-2.7	4					63	69	48	64					3938	4062	3941	4336					1524	1647	1208	1545
5	IW-2.3	5.9							53	63							4075	4315							1315	1524
6	IW-2.1	8							56	63							4151	4315							1378	1524
7	IW-1.9	10							57	62							4175	4292							1399	1503
8	IW-1.7	12							59	62							4223	4292							1441	1503
9	IW-1.4	17							60	60							4264	4264							1462	1462
10	IW-1.3	18							60	60							4264	4264							1462	1462
11	IW-1.2	22							59	60							4223	4264							1441	1462
12	IW-1.0	27							57	58							4175	4199							1399	1420
13	IW-0.8	34							55	55							4126	4126							1357	1357
14	IW-0.6	43							50	52							3996	4049							1251	1294

			Magma Ocean Pressure (average at end of accretion) (GPa)								Magma Ocean Temperature (average at end of accretion) (K)							
Path	Initial Redox	Initial FeO (mol%)	Solidus		Cool Liquidus		Average Liquidus		Hot Liquidus		Solidus		Cool Liquidus		Average Liquidus		Hot Liquidus	
1	IW-4.5	0.6	30	45	29	45	28	43	26	39	2571	2941	2778	3142	2998	3409	3184	3615
2	IW-4.5	0.6	40	45	33	45	27	43	26	39	2822	2941	2866	3142	2980	3409	3184	3597
3	IW-3.3	2			44	44	32	42	25	39			3128	3128	3121	3394	3162	3597
4	IW-2.7	4					38	42	29	39					3286	3379	3290	3597
5	IW-2.3	5.9							32	38							3392	3580
6	IW-2.1	8							34	38							3450	3580
7	IW-1.9	10							34	38							3469	3562
8	IW-1.7	12							36	38							3507	3562
9	IW-1.4	17							36	36							3525	3525
10	IW-1.3	18							36	36							3525	3525
11	IW-1.2	22							36	36							3507	3525
12	IW-1.0	27							34	35							3469	3488
13	IW-0.8	34							33	33							3431	3413
14	IW-0.6	43							30	31							3332	3372

			Core Oxygen Content (wt%)								Core Silicon Content (wt%)								Core Light Element Content (wt%)							
Path	Initial Redox	Initial FeO (mol%)	Solidus		Cool Liquidus		Average Liquidus		Hot Liquidus		Solidus		Cool Liquidus		Average Liquidus		Hot Liquidus		Solidus		Cool Liquidus		Average Liquidus		Hot Liquidus	
1	IW-4.5	0.6	0.3%	0.7%	0.5%	1.0%	0.7%	1.6%	1.1%	2.5%	2.4%	4.9%	3.9%	6.6%	5.6%	9.0%	7.1%	11.2%	2.7%	5.6%	4.4%	7.6%	6.3%	10.6%	8.2%	13.7%
2	IW-4.5	0.6	0.6%	0.8%	0.6%	1.0%	0.8%	1.7%	1.1%	2.4%	2.6%	3.2%	2.9%	4.6%	3.6%	6.6%	5.0%	8.4%	3.2%	4.0%	3.5%	5.6%	4.4%	8.3%	6.1%	10.8%
3	IW-3.3	2			1.1%	1.1%	1.1%	1.7%	1.2%	2.5%			3.3%	3.3%	3.4%	5.0%	3.6%	6.6%			4.4%	4.4%	4.5%	6.7%	4.8%	9.1%
4	IW-2.7	4					1.6%	1.8%	1.6%	2.7%					3.5%	3.9%	3.5%	5.4%					5.1%	5.7%	5.1%	8.1%
5	IW-2.3	5.9							2.0%	2.8%							3.5%	4.6%							5.5%	7.4%
6	IW-2.1	8							2.4%	3.0%							3.4%	4.1%							5.8%	7.1%
7	IW-1.9	10							2.7%	3.1%							3.1%	3.6%							5.8%	6.7%
8	IW-1.7	12							3.1%	3.4%							3.0%	3.3%							6.1%	6.7%
9	IW-1.4	17							3.8%	3.8%							2.7%	2.7%							6.5%	6.5%
10	IW-1.3	18							3.9%	3.9%							2.6%	2.6%							6.5%	6.5%
11	IW-1.2	22							4.4%	4.5%							2.3%	2.3%							6.7%	6.8%
12	IW-1.0	27							4.9%	5.1%							2.3%	2.0%							7.2%	7.1%
13	IW-0.8	34							5.8%	5.8%							1.6%	1.6%							7.4%	7.4%
14	IW-0.6	43							6.6%	7.1%							1.2%	1.3%							7.8%	8.4%

2. Core Light-Element Content

It is obvious that any proposed compositional model for the core must (at the very least) match – within uncertainties – the seismically observed density and sound velocity of the core. The idea here is to rule out core composition models based on their Si and O concentration; for this we need to define the broadest O–Si solution space that is compatible with seismology. This analysis has only been possible recently possible (4) thanks to first principles molecular dynamics simulation, offsetting the lack of density and velocity data on (Fe–Ni)–C–O–Si–S liquid alloys under core conditions. Measuring bulk sound velocities and densities in molten Fe alloys at core conditions lies currently beyond the capability of experimentation. An alternative is to use *ab initio* simulations to interpret seismic observations in terms of outer core composition. We can, therefore, calculate the density and bulk sound velocity of liquid alloys in the (Fe–Ni)–C–O–Si–S system using *ab initio* molecular dynamics. We then compare the properties of the molten alloys directly with the primary geophysical observations, *e.g.* density and bulk sound velocity obtained from radial seismic models (5, 6); keeping only the ones that satisfy seismology. This subset of compositions defines a seismologically constrained compositional model of the Earth's core.

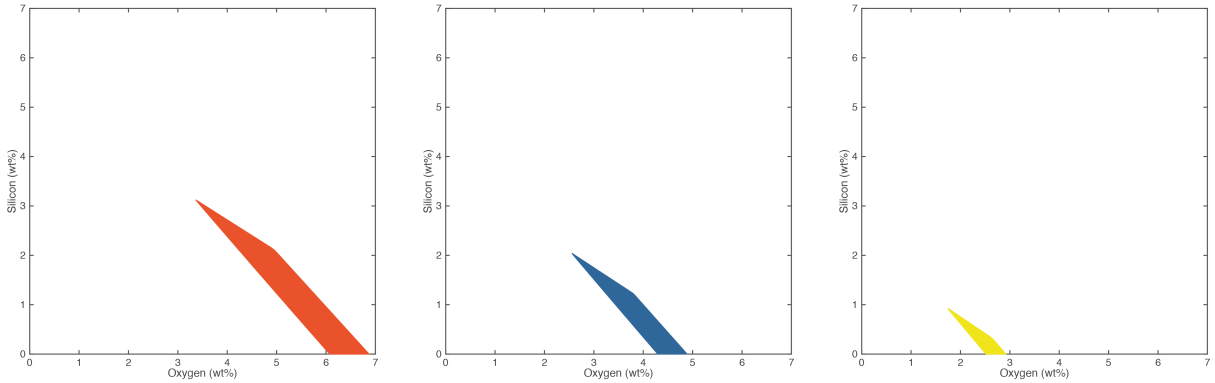

Figure S4: The three panels show plots of the Si–O concentration range that is consistent with the AK135 seismological model, for three fixed S- and C- concentrations. At the left is the end-member with no S nor C. In the middle, a model with 1 wt% S and 1wt% C. At the right a model with 2% S and 2% C.

We chose the AK135 (6) radial seismic model, and corrected the velocity profile to avoid artifacts from the F-layer and the low-velocity layer at the CMB. In all simulations, the Ni content was fixed (7) at 4.2%. First we calculated the O–Si solution maps for fixed amounts of S and C, according to (4). Figure S4 shows three such solution maps.

As we said earlier, ruling out core composition models based on their Si and O concentration requires defining the broadest O–Si solution space. For this, we need to superpose the individual O–Si solution maps calculated for all possible/plausible S and C concentrations. This superposition map is shown in figure S5, and has been calculated for all C and S concentrations between 0 and 7 wt% and 0 and 3 wt%, respecitvely. The 3% sulfur limit was taken from the cosmochemical arguments put forth in (8).

To give the readers a more granular perception of the distinctive effects of S and C on figure S5, we plotted O–Si core concentrations for four core concentrations of sulfur: 0%, 1%, 2% and 3%.

The results are reported in figure S6, and the area in each subplot represents the broadest O–Si solution space for its associated sulfur concentration, with the C concentration indicated by the color of the symbol. One can see figure S5 as the superposition of individual figures similar to the ones in figure S6, calculated for a discrete range of S concentrations.

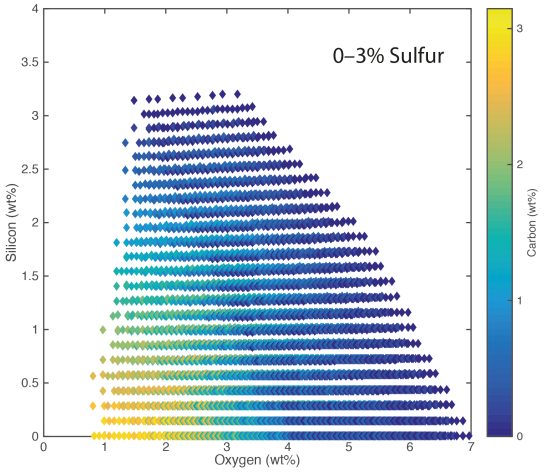

Figure S5: The O–Si concentration range consistent with the AK135 radial seismic model, for any sulfur concentration between 0 and 3% and any carbon concentration. The symbol color is mapped to carbon concentration with the scale in the color bar to the right.

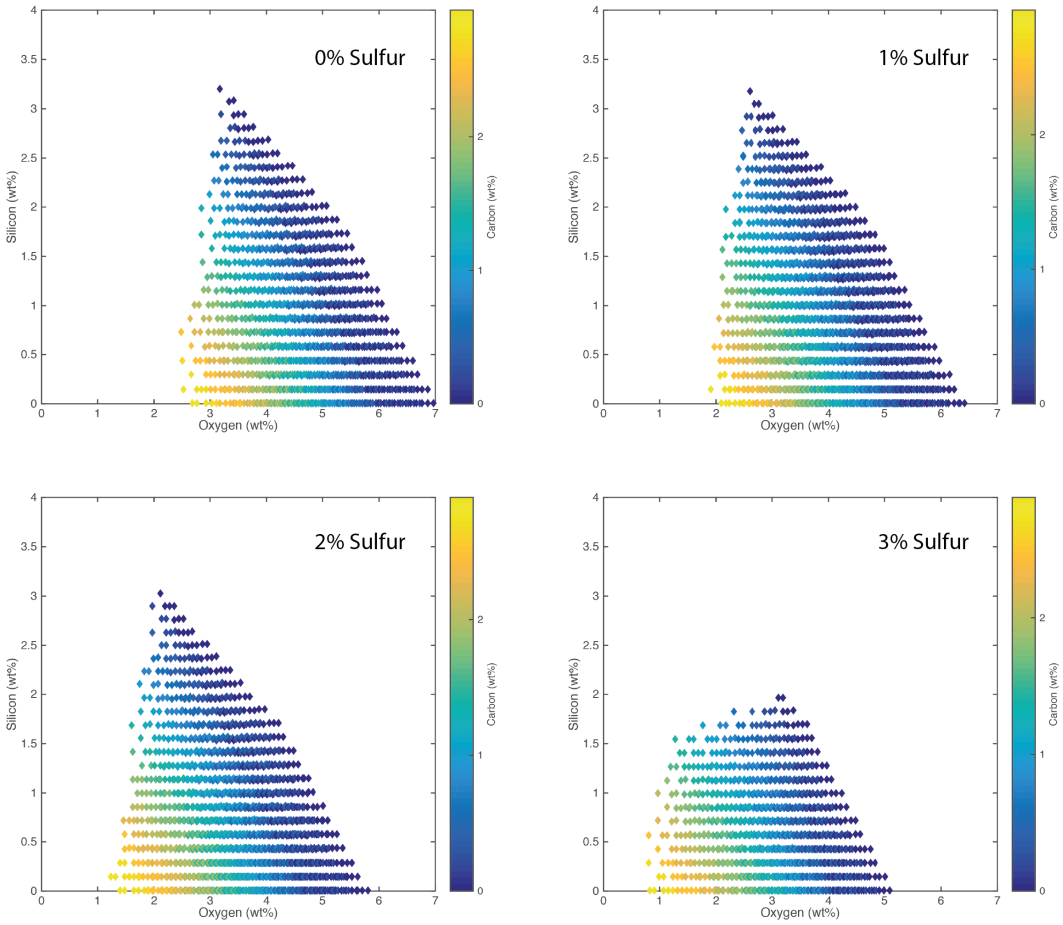

Figure S6: The O–Si–C concentration range consistent with the AK135 radial seismic model, for four sulfur concentrations: 0% (upper left), 1% (upper right), 2% (lower left), and 3% (lower right). Symbol color is mapped to carbon concentration with the scale in the color bar to the right of each graph.

3. References

1. Ma ZT (2001) Thermodynamic description for concentrated metallic solutions using interaction parameters. *Metallurgical and Materials Transactions B-Process Metallurgy and Materials Processing Science* 32(1):87-103.
2. Siebert J, Badro J, Antonangeli D, & Ryerson FJ (2013) Terrestrial Accretion Under Oxidizing Conditions. *Science*.
3. Siebert J, Badro J, Antonangeli D, & Ryerson FJ (2012) Metal-silicate partitioning of Ni and Co in a deep magma ocean. *Earth and Planetary Science Letters* 321:189-197.
4. Badro J, Cote AS, & Brodholt JP (2014) A seismologically consistent compositional model of Earth's core. *Proceedings of the National Academy of Sciences of the United States of America* 111(21):7542-7545.
5. Dziewonsky AM & Anderson DL (1981) Preliminary reference Earth model. *Physics of the Earth and Planetary Interiors* 25:297-356.
6. Kennett BLN, Engdahl ER, & Buland R (1995) Constraints on Seismic Velocities in the Earth from Travel-Times. *Geophysical Journal International* 122(1):108-124.
7. Allegre CJ, Poirier JP, Humler E, & Hofmann AW (1995) The Chemical-Composition of the Earth. *Earth and Planetary Science Letters* 134(3-4):515-526.
8. Dreibus G & Palme H (1996) Cosmochemical constraints on the sulfur content in the Earth's core. *Geochimica Et Cosmochimica Acta* 60(7):1125-1130.